Electronic Supplementary Material (ESI) for Dalton Transactions

Spin crossover in di-, tri- and tetranuclear, mixed-ligand tris(pyrazolyl)methane iron(II) complexes.

Caspar J. Schneider,[a] Boujemaa Moubaraki,[a] John D. Cashion,[b] David R. Turner,[a] Benjamin A. Leita,[a] Stuart R. Batten[a] and Keith S. Murray[a*]

ELECTRONIC SUPPLEMENTARY INFORMATION

Fig. S1 Crystal packing in **1**·2DME looking down the *c* axis

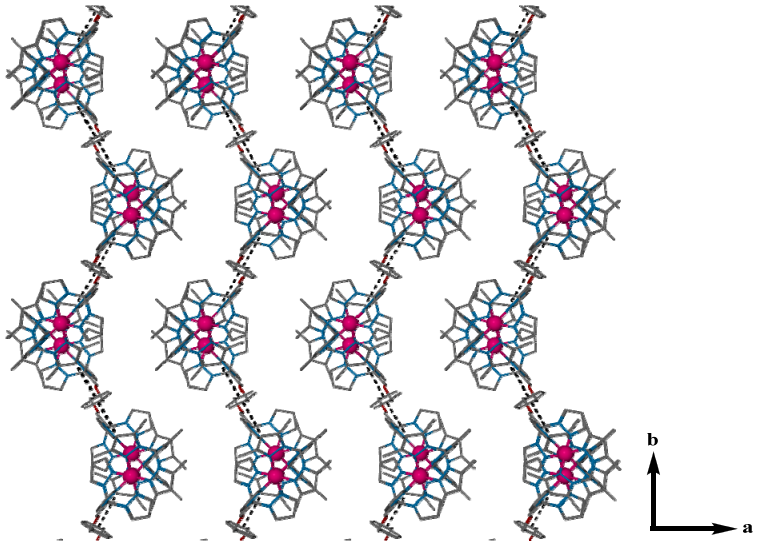

Fig. S2 . Two perspectives of the orientation of the DME solvent molecules (space filling) in regard to the naphthalene core in **2**·2.5MeCN.2DME. (a) perpendicular (b) parallel

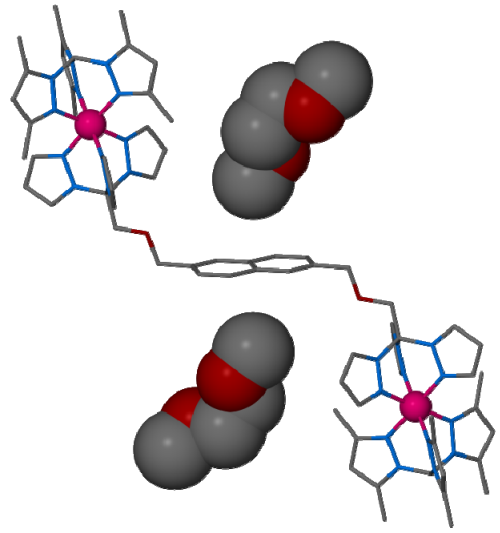

(a)

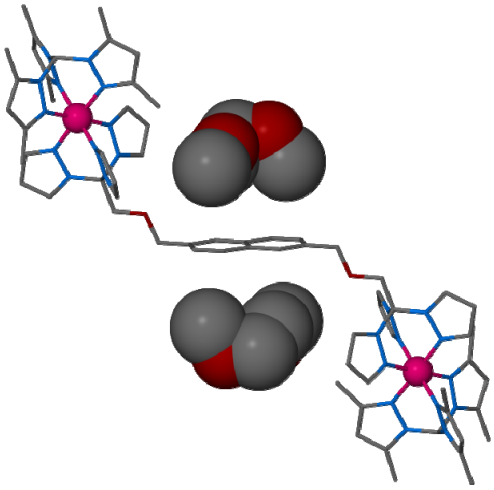

(b)

Fig. S3 Structure of the dinuclear complex cation in **3**·2DME

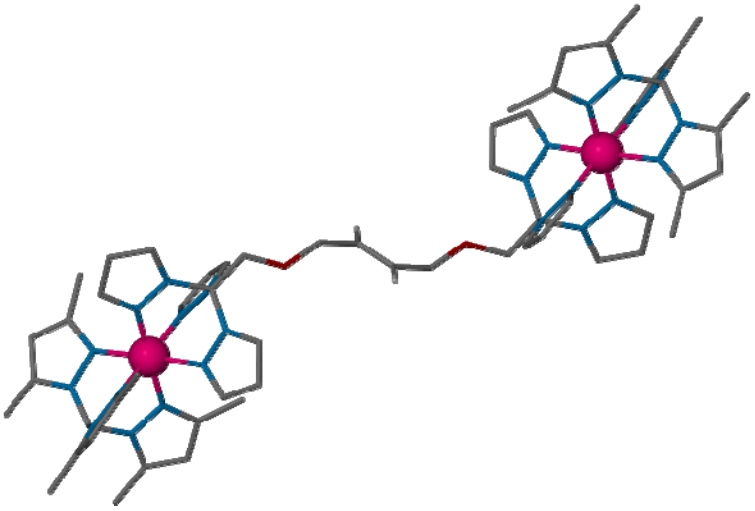

Fig. S4. BF_4^- to trimer interactions within 'capsules' of **4**.solvent

The dotted lines represent the CH..F interactions with H to F distances of 2.12 to 2.26 Å

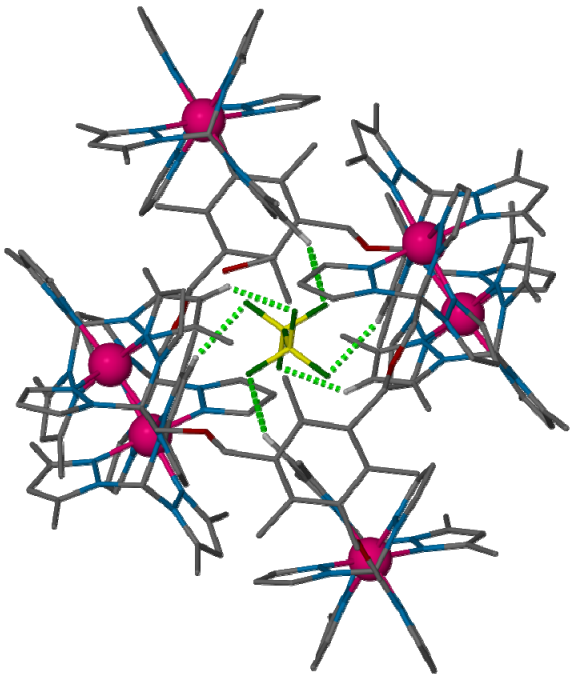

Fig. S5 Magnetic Susceptibilty, $\chi_M T$, data for **1**·2DME obtained by careful thermal cycling between 200 and 375 K. The rhs plot is cycle 1, warming **1**·2DME from 200 to 375 K. The other plots are cycles 2 and 3, cooling and warming, for **1** that is formed after cycle 1. The next data point for **1.**2DME at high temperature lies on the plot for **1**. The hysteresis in **1** (see script) is clearly reproducible at ~330 K.

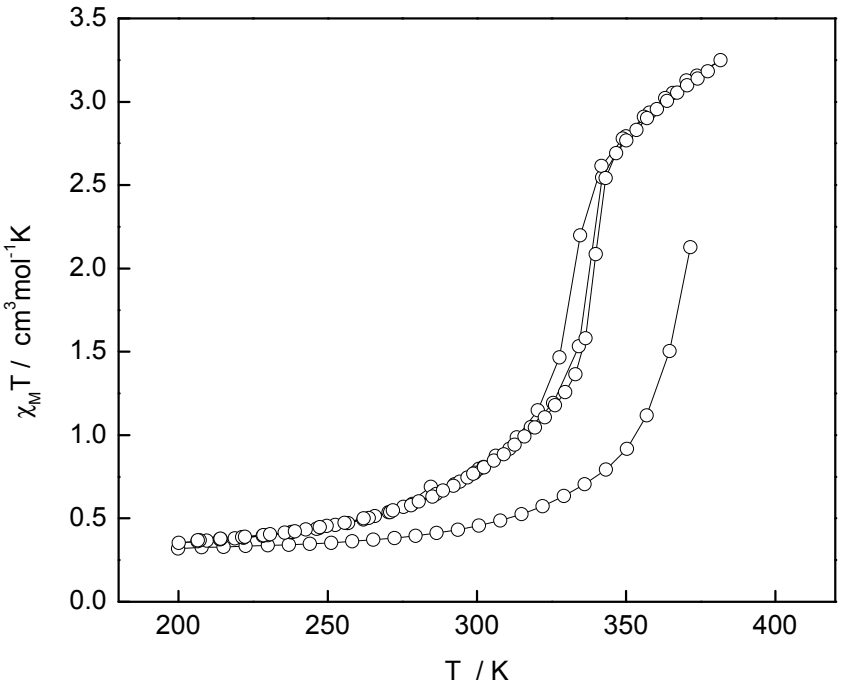

Fig. S6 Magnetic Susceptibilty data for **1**·6MeCN. Data plotted as $\chi_M T$, per Fe

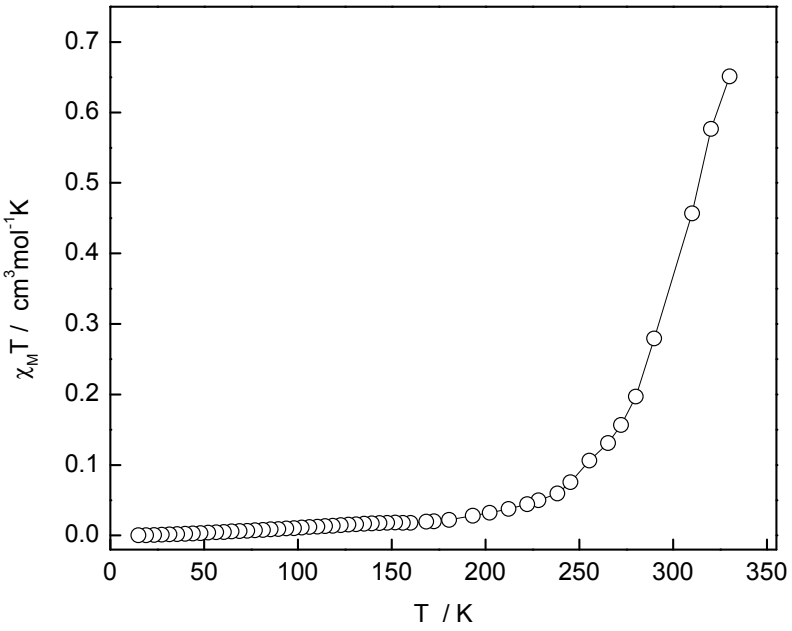

Fig. S7 Thermogravimetric analytical (TGA) data collected on **1**·2DME

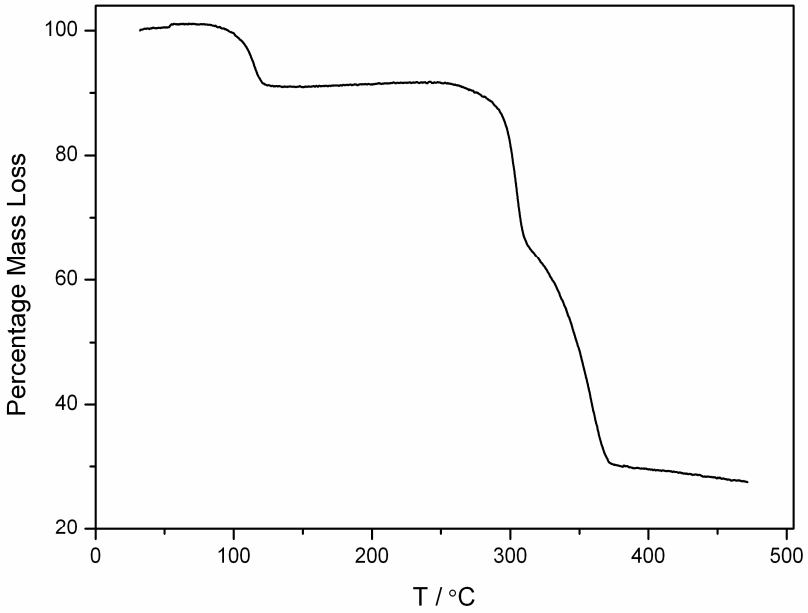

Fig. S8 Thermogravimetric data collected on **3**·2DME

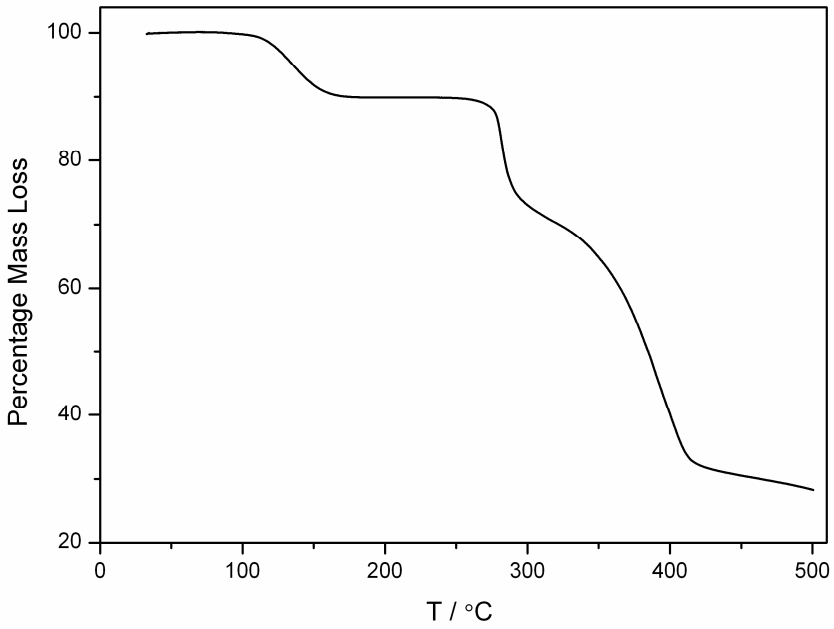

Fig. S9 Thermogravimetric data collected on **5**·8MeCN.2^{t}BuOMe

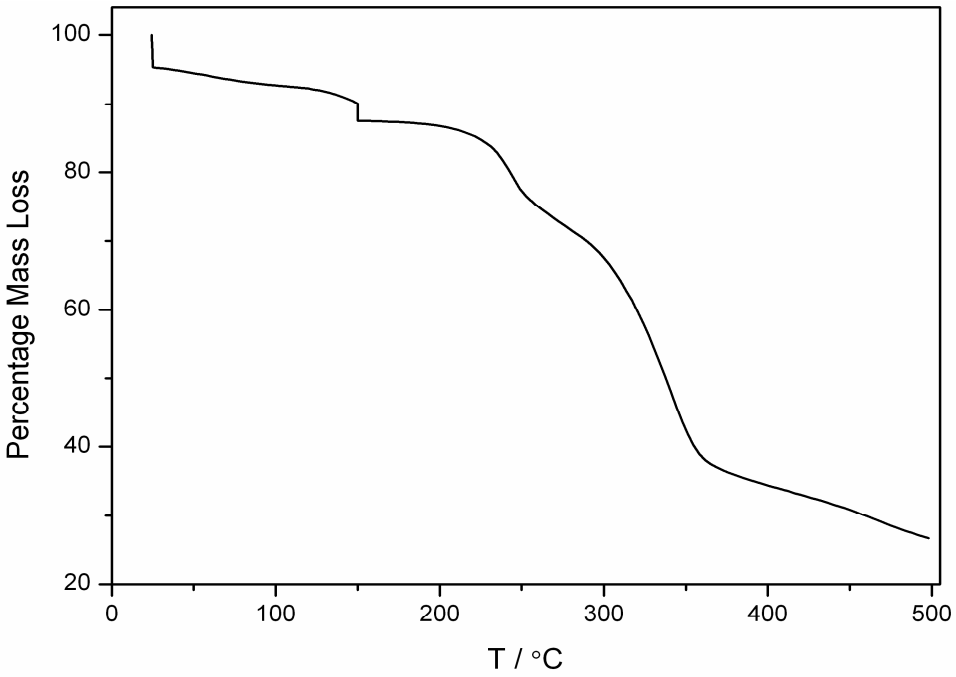

Fig. S10 Le Bail refinement for **1**·2DME at 220 K

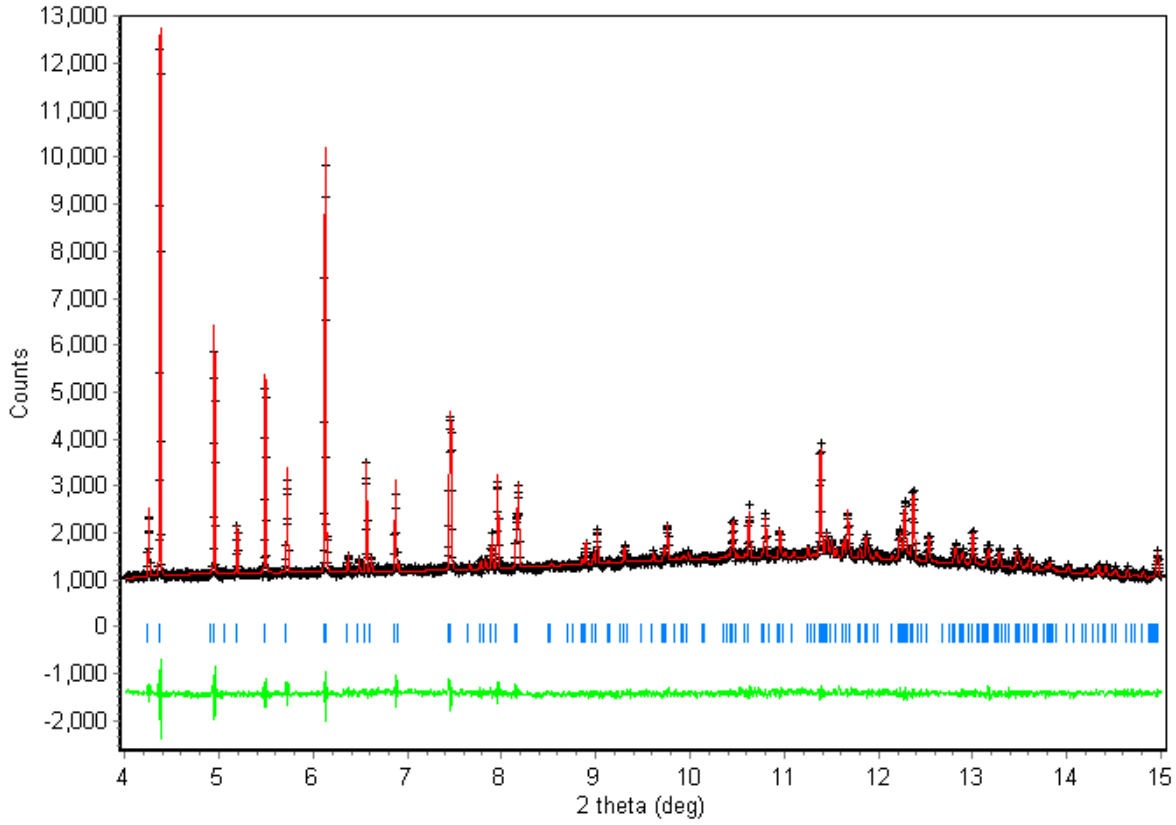

Fig. S11. Variable temperature cell axes lengths *a* (top), *b* to *c*, *β* angle and unit cell volume, *V* (bottom), for **1**.2DME. The 'glitches' at 250 and 330 K, on warming, are instrumental in origin.

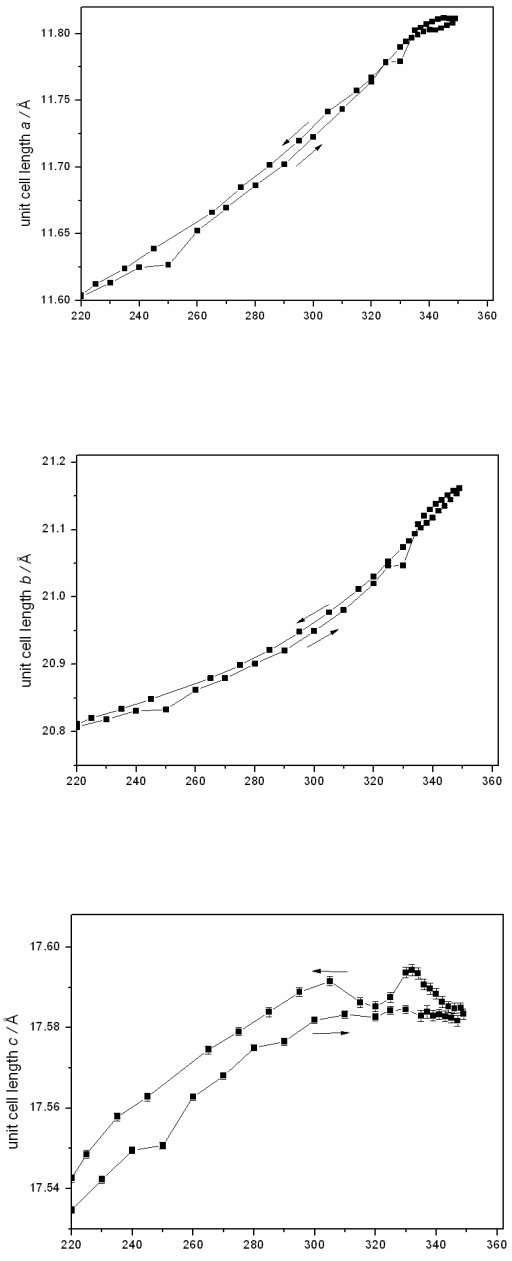

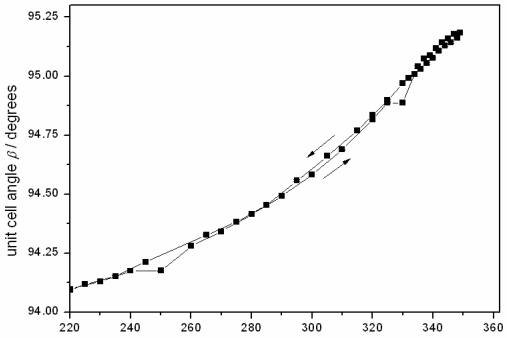

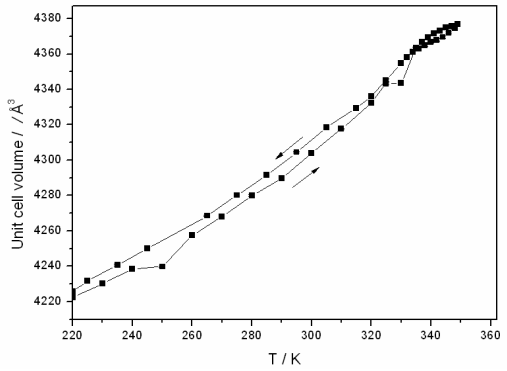

Table S1. Summary of crystallographic parameters for **1**·2DME (at 123 K, 173 K, 223 K and 273 K), **2**·3MeCN.2DME, **3**·2DME and **5**·8MeCN.2^{t}BuOMe

	1•2DME	**1**•2DME	**1**•2DME	**1**•2DME
Formula	$C_{70}H_{94}B_4F_{16}Fe_2N_{24}O_6$	$C_{70}H_{94}B_4F_{16}Fe_2N_{24}O_6$	$C_{70}H_{94}B_4F_{16}Fe_2N_{24}O_6$	$C_{70}H_{94}B_4F_{16}Fe_2N_{24}O_6$
M	1826.63	1826.63	1826.63	1826.63
Crystal System	Monoclinic	Monoclinic	Monoclinic	Monoclinic
Space Group	$P2_1/c$	$P2_1/c$	$P2_1/c$	$P2_1/c$
a/ Å	11.5038(3)	11.5446(5)	11.6011(10)	11.632(3)
b/ Å	20.7090(6)	20.7555(11)	20.802(2)	20.824(5)
c/ Å	17.4235(5)	17.4704(9)	17.4828(17)	17.456(4)
α/°	90	90	90	90
ß/°	93.935(2)	93.932(2)	94.192(4)	94.407(13)
γ/°	90	90	90	90
V/ Å^3	4141.1(2)	4176.3(4)	4207.7(7)	4215.9(17)
Z	2	2	2	2
T(K)	123(2)	173(2)	223(2)	273(2)
θ_{max}	27.50	25.16	27.50	27.50
Measured Reflections	26328	22188	40611	32852
Unique Reflections	9475	7065	9468	9660
Observed Reflections	7271	5181	6147	5154
Final *GoF*	1.142	1.044	1.025	1.029
R1[a]	0.0735	0.0535	0.0667	0.0751
wR2[a]	0.1286	0.1366	0.1609	0.1795

	2•2.5MeCN.2DME	**3**•2DME	**5**•8MeCN.2^{t}BuOMe
Formula	$C_{79}H_{103.50}B_4F_{16}Fe_2N_{26.50}O_6$	$C_{66}H_{92}B_4F_{16}Fe_2N_{24}O_6$	$C_{144}H_{190}B_8F_{32}Fe_4N_{56}O_6$
M	1979.32	1776.58	3719.40
Crystal System	Triclinic	Monoclinic	Monoclinic
Space Group	P-1	$P2_1/c$	$P2_1/n$
a/ Å	14.1238(6)	11.1486(7)	15.3526(9)
b/ Å	16.4661(9)	21.4040(15)	17.5492(12)
c/ Å	23.0010(12)	16.9246(10)	32.453(2)
α/°	69.346(3)	90	90
ß/°	82.768(3)	92.734(2)	99.077(2)
γ/°	70.093(3)	90	90
V/ Å^3	4706.2(4)	4034.0(4)	8634.3(10)
Z	2	2	2
T(K)	123(2)	123(2)	123(2)
θ_{max}	25	27.50	27.50
Measured Reflections	93505	32487	53029
Unique Reflections	16557	9141	19201
Observed Reflections	11410	7430	9353
Final *GoF*	1.026	1.194	1.045
R1[a]	0.0740	0.0752	0.0979
wR2[a]	0.2059	0.1566	0.2669

[a] $R1 = \Sigma||F_o| - |F_c||/\Sigma|F_o|$, $wR2 = \{\Sigma[w(F_o^2\Sigma F_c^2)^2]/\Sigma[w(F_o^2)^2]\}^{1/2}$

Table S2. Selected Fe-N bond lengths (Å),[a] N-Fe-N bond angles (°), Fe-N-N-C torsion angles (°), intra/ internuclear Fe---Fe distances (Å) for compounds **1**·2DME, **2**·2.5MeCN.2DME, **3**·2DME and **5**·8MeCN.2^{t}BuOMe. See Scheme 1 for atom numbering.

	1·2DME 123 K	**1**·2DME 173 K	**1**·2DME 223 K	**1**·2DME 273 K	**2**·2.5MeCN.2DME 123 K	**3**·2DME 123K	**5**·8MeCN.2^{t}BuOMe 123K
Fe(1)-N(2)	1.956(3)	1.959(3)	1.952(3)	1.946(4)	1.946(3)	1.953(3)	1.963(5)
Fe(1)-N(4)	1.943(3)	1.942(3)	1.942(3)	1.936(3)	1.933(4)	1.951(3)	1.942(5)
Fe(1)-N(6)	1.954(3)	1.950(3)	1.950(3)	1.946(3)	1.943(4)	1.953(3)	1.966(5)
Fe(1)-N(7)	1.995(3)	2.000(3)	2.001(3)	1.993(3)	1.973(3)	1.999(3)	2.002(5)
Fe(1)-N(9)	1.971(3)	1.979(3)	1.975(3)	1.968(3)	1.979(3)	1.982(3)	1.993(5)
Fe(1)-N(11)	1.984(3)	1.985(3)	1.986(3)	1.978(3)	1.982(4)	1.991(3)	1.993(5)
Cis N-Fe-N angles							
N(2)-Fe(1)-N(4)	86.59(12)	86.68(11)	86.72(12)	86.46(14)	88.08(15)	86.95(11)	86.7(2)
N(2)-Fe(1)-N(6)	86.91(12)	87.21(11)	87.09(12)	87.02(14)	86.54(15)	86.17(12)	87.6(2)
N(2)-Fe(1)-N(7)	94.05(12)	93.83(11)	93.66(12)	93.45(14)	90.99(14)	93.50(11)	93.6(2)
N(2)-Fe(1)-N(11)	94.39(12)	94.18(12)	94.07(12)	94.46(15)	93.50(15)	94.69(12)	92.6(2)
N(4)-Fe(1)-N(6)	88.77(12)	88.76(11)	88.62(11)	88.60(14)	87.91(15)	88.74(12)	88.4(2)
N(4)-Fe(1)-N(7)	91.02(12)	91.14(11)	91.40(11)	91.58(14)	90.23(15)	90.54(11)	92.3(2)
N(4)-Fe(1)-N(9)	91.59(12)	91.51(11)	91.27(12)	91.36(14)	91.21(15)	91.41(11)	91.7(2)
N(6)-Fe(1)-N(9)	90.47(12)	90.27(11)	90.59(11)	90.78(14)	92.58(15)	91.07(12)	89.5(2)
N(6)-Fe(1)-N(11)	91.27(13)	91.40(11)	91.48(11)	91.67(14)	93.65(15)	92.43(12)	91.6(2)
N(7)-Fe(1)-N(9)	88.56(12)	88.69(11)	88.66(11)	88.76(14)	89.86(14)	89.25(11)	89.3(2)
N(7)-Fe(1)-N(11)	88.92(13)	88.69(12)	88.50(11)	88.15(14)	88.27(15)	88.29(11)	87.7(2)
N(9)-Fe(1)-N(11)	87.44(12)	87.64(11)	87.94(12)	87.73(14)	87.24(15)	87.01(12)	89.0(2)
Trans N-Fe-N angles							
N(2)-Fe(1)-N(9)	176.84(13)	176.92(11)	176.96(11)	176.94(15)	178.89(15)	176.81(12)	176.7(2)
N(4)-Fe(1)-N(11)	179.02(12)	179.13(12)	179.21(13)	179.05(14)	177.84(15)	178.04(12)	179.3(2)
N(6)-Fe(1)-N(7)	179.01(12)	178.95(12)	179.25(12)	179.51(14)	176.97(14)	179.22(11)	178.6(2)
Torsion Fe-N-N-C angles							
Fe(1)-N(7)-N(8)-C(16)	1.9(4)	1.4(4)	0.9(4)	1.1(5)	0.7(5)	0.2(4)	6.5(6)
Fe(1)-N(9)-N(10)-C(16)	0.7(4)	0.8(3)	0.5(3)	1.6(4)	5.0(5)	5.6(3)	2.3(7)
Fe(1)-N(11)-N(12)-C(16)	3.8(4)	2.3(4)	2.3(4)	1.8(4)	1.3(4)	1.8(4)	2.6(7)
Fe(1)-N(2)-N(1)-C(26)	3.4(4)	3.2(4)	3.1(4)	2.2(5)	4.6(5)	5.2(4)	3.8(7)
Fe(1)-N(4)-N(3)-C(26)	7.4(4)	7.5(4)	6.8(4)	6.5(4)	1.9(5)	8.7(3)	2.9(6)
Fe(1)-N(6)-N(5)-C(26)	1.3(4)	2.0(3)	1.6(4)	1.2(4)	0.1(5)	1.6(4)	1.8(7)
Intra/Internuclear Fe---Fe distances							
Fe---Fe DIST 1 [b]	16.362(1)	16.400(1)	16.404(2)	16.390(3)	18.311 (1)	15.441(1)	10.227 (2)
Fe---Fe DIST 2 [c]	8.888(1)	8.915(1)	8.922 (1)	8.907(2)	10.887(1)	8.726(1)	9.313 (2)
Fe---Fe DIST 3 [d]	14.121(1)	14.183(1)	14.252(2) (	14.291(3)	----	14.812(1)	----

[a]Values for Fe(1) are presented. Fe(1) is characteristic of all the iron(II) centre geometries within the structure. [b] DIST 1 is the shortest intranuclear distance between iron(II) centres in a single complex. [c] DIST 2 is the shortest internuclear distance between iron(II) centres. [d] DIST 3 is the internuclear distance between iron(II) centres that are involved in C-H---π interactions (applies to **3**·2DME that does not have the C-H---π interaction

Table S3. Crystallographic parameters for **1**·6MeCN at 173 K

Formula	$C_{74}H_{92}B_4F_{16}Fe_2N_{30}O_2$
M	1892.72
Crystal System	Triclinic
Space Group	P-1
a/ Å	13.451(3)
b/ Å	14.795(3)
c/ Å	15.885(3)
α/°	116.03(3)
ß/°	104.63(3)
γ/°	94.23(3)
V/ Å^3	2685.8(10)
Z	1
T(K)	173(2)
θ_{max}	27.50
Measured Reflections	26431
Unique Reflections	11833
Observed Reflections	4531
Final *GoF*	1.249
R1[a]	0.1583
wR2[a]	0.4585

Table S4. Selected Fe-N bond lengths (Å), N-Fe-N bond angles (°) and Fe-N-N-C torsion angles (°) for compounds **1**·6MeCN

Fe(1)-N(2)	1.947(7)
Fe(1)-N(4)	1.914(7)
Fe(1)-N(6)	1.945(7)
Fe(1)-N(7)	1.979(7)
Fe(1)-N(9)	1.991(7)
Fe(1)-N(11)	1.979(7)
Cis N-Fe-N angles	
N(2)-Fe(1)-N(4)	87.9(3)
N(2)-Fe(1)-N(6)	87.1(3)
N(2)-Fe(1)-N(7)	91.0(3)
N(2)-Fe(1)-N(11)	92.7(3)
N(4)-Fe(1)-N(6)	87.4(3)
N(4)-Fe(1)-N(7)	91.4(3)
N(4)-Fe(1)-N(9)	91.4(3)
N(6)-Fe(1)-N(9)	92.2(3)
N(6)-Fe(1)-N(11)	93.1(3)
N(7)-Fe(1)-N(9)	89.8(3)
N(7)-Fe(1)-N(11)	88.1(3)
N(9)-Fe(1)-N(11)	88.0(3)
Trans N-Fe-N angles	
N(2)-Fe(1)-N(9)	179.0(3)
N(4)-Fe(1)-N(11)	179.2(3)
N(6)-Fe(1)-N(7)	177.8(3)
Torsion Fe-N-N-C angles	
Fe(1)-N(7)-N(8)-C(16)	3.2(9)
Fe(1)-N(9)-N(10)-C(16)	0.7(9)
Fe(1)-N(11)-N(12)-C(16)	0.6(9)
Fe(1)-N(2)-N(1)-C(26)	2.4(9)
Fe(1)-N(4)-N(3)-C(26)	2.2(9)
Fe(1)-N(6)-N(5)-C(26)	3.7(10)

Table S5 Summary of crystallographic parameters for **4**·Solvent

	100 K	**220 K**
Formula	$C_{93}H_{117}B_6F_{24}Fe_3N_{36}O_{3.75}$	$C_{93}H_{117}B_6F_{24}Fe_3N_{36}O_{3.75}$
M	2487.64	2487.64
Crystal System	Triclinic	Triclinic
Space Group	P-1	P-1
a/ Å	23.066(4)	23.163(8)
b/ Å	23.150(6)	23.362(8)
c/ Å	23.968(4)	24.048(6)
α/°	77.782(7)	77.637(16)
β/°	83.522(20)	83.250(30)
γ/°	83.411(21)	83.232(16)
V/ Å^3	12374(4)	12566(7)
Z	4	4
T(K)	100(2)	220(2)
θ_{max}	25.62	27.18
Measured Reflections	128846	149112
Unique Reflections	33012	48008
Observed Reflections	15688	20562
Final *GoF*	1.751	1.435
R1[a]	0.1460	0.1330
wR2[a]	0.3616	0.3421

[a] $R1 = \Sigma||F_o| - |F_c||/\Sigma|F_o|$, $wR2 = \{\Sigma[w(F_o^2\Sigma F_c^2)^2]/\Sigma[w(F_o^2)^2]\}^{1/2}$

Table S6 Selected Fe-N bond lengths (Å),[a] N-Fe-N bond angles (°), Fe-N-N-C torsion angles (°) and intra-nuclear Fe---Fe distances (Å) for the trinuclear compound **4**.solvent.

	100 K	**220 K**
Fe(1)-N(2)	1.957(9)	1.939(6)
Fe(1)-N(4)	1.921(11)	1.920(7)
Fe(1)-N(6)	1.967(8)	1.973(6)
Fe(1)-N(7)	2.001(9)	2.008(6)
Fe(1)-N(9)	1.976(8)	1.981(6)
Fe(1)-N(11)	2.010(11)	2.000(7)
Cis N-Fe-N angles		
N(2)-Fe(1)-N(4)	87.8(4)	87.4(3)
N(2)-Fe(1)-N(6)	86.7(3)	87.3(2)
N(2)-Fe(1)-N(7)	90.8(4)	91.4(2)
N(2)-Fe(1)-N(11)	91.6(4)	91.8(3)
N(4)-Fe(1)-N(6)	87.8(4)	87.4(2)
N(4)-Fe(1)-N(7)	92.9(4)	92.7(3)
N(4)-Fe(1)-N(9)	91.8(4)	92.2(3)
N(6)-Fe(1)-N(9)	94.3(4)	92.9(2)
N(6)-Fe(1)-N(11)	90.3(4)	91.4(2)
N(7)-Fe(1)-N(9)	88.3(4)	88.3(2)
N(7)-Fe(1)-N(11)	88.9(4)	88.5(3)
N(9)-Fe(1)-N(11)	88.8(4)	88.6(2)
Trans N-Fe-N angles		
N(2)-Fe(1)-N(9)	179.0(4)	179.5(3)
N(4)-Fe(1)-N(11)	178.1(4)	178.6(2)
N(6)-Fe(1)-N(7)	177.4(4)	178.7(2)
Torsion Fe-N-N-C angles		
Fe(1)-N(7)-N(8)-C(34)	2.1(15)	2.6(9)
Fe(1)-N(9)-N(10)-C(34)	1.5(13)	2.2(8)
Fe(1)-N(11)-N(12)-C(34)	1.9(11)	1.8(8)
Fe(1)-N(2)-N(1)-C(9)	6.1(13)	4.4(8)
Fe(1)-N(4)-N(3)-C(9)	6.2(12)	6.3(8)
Fe(1)-N(6)-N(5)-C(9)	1.2(14)	2.4(8)
Intra/internuclear Fe---Fe distances		
Fe---Fe DIST 1[b]	10.149(3)	10.169(4)
	9.972(4)	10.010(3)
	10.062(4)	10.105(3)
Fe---Fe DIST 2[c]	8.879(3)	8.930(3)

[a] Values for Fe(1) are presented and display no significant differences from the other iron(II) centre geometries present within the structure. [b]DIST 1 = intra-nuclear distances. [c] DIST 2 = nearest inter-nuclear distance. Fe---Fe distances between capsular units ~10.3 Å. Please **note** that compared to the other structures, C34 is equivalent to C16 and C9 equivalent to C26 (Scheme 1 and cif)

Crystallographic details for the trinuclear (capsular) complex 4

The two crystallographically unique halves of the 'capsules' appear to contain partial occupancy solvent close to the hexa-substituted benzene rings, with a single water position refined in one instance and two disordered water positions in the other. Hydrogen atoms were not modelled for these solvent molecules. Only ten tetrafluoroborate counter-anions could be located from the Fourier difference map. These lie either within or close to the outer surface of the capsules and are therefore reasonably well-ordered. It is believed that the remaining counter-anions lie within the pore space and are too disordered to observe, alongside further disordered lattice solvent. The anions within the capsule are located close to centre of the cavity with one anion disordered across the crystallographic inversion centre in each case. Nine of the anions were refined either with SADI restraints applied to the B-F and F···F distances or with the SAME geometry as a restrained anion. The remaining anion (labelled K) is disordered around the boron atom and is freely refined with an approximate trigonal bipyramidal geometry that best represents the overlay of the two positions. Some of the anions were refined using an isotropic model due to excessively large displacement parameters. It appears that these anions have further rotational disorder, however, this could not be modelled. In the lower temperature structure five atoms required the use of the ISOR restraint due to poor behaviour of the anisotropic parameters during refinement (B1A, B1C, B1D, N21, C81). No geometrical restraints were applied to the cationic complexes. One of the arms of one of the tripodal complexes is apparently disorder, evidenced by large displacement parameters in one direction that increase in magnitude approaching the tip of the arm. Disorder could not be modelled for this situation and the large ellipsoids remain in the model as the best descriptor for the structure of the complex.

Both datasets were treated with the SQUEEZE routine of PLATON due to the large amount of residual electron density within the pores of the structure that could not be modelled. There is a calculated void volume of 2142 $Å^3$ per unit cell with an electron count of 772 for the 100 K data

and 2164 $Å^3$ / 729 e^- for the 220 K data (i.e. reasonably good agreement between the two samples). Some moderately sized areas of electron density remain in the Fourier difference map within and between the 'capsules' although these could not be modelled and may represent further areas of disordered solvent molecules.

Further notes on molecular structure and intermolecular interactions in some of the complexes

1.2DME

The BF_4^- anions and DME solvent molecules, in **1**·2DME, are located in the spaces between the 2D sheets and facilitate, via hydrogen bonding, assembly of the overall 3D lattice structure. Numerous weak C-H---F hydrogen-bond interactions occur between the BF_4^- anions and the hydrogen atoms of the pyrazolyl ring and ether-linked arms of the ligand. The DME solvent molecules, which interact weakly with the dinuclear cation as a hydrogen bond acceptor, play an important role in determining the crystal packing.

2.2.5MeCN.2DME

The dinuclear units shown in ESI Fig. S2 also display a similar *transoid* arrangement, with regard to the plane of the naphthalene ring system, to that observed for the 1,4-xylene moiety in **1**·2DME.

Both DME and MeCN solvent molecules are observed in the crystal lattice of **2**·2.5MeCN.2DME. In particular, there are two different orientations for the DME solvent molecules located in the hydrophobic pocket provided primarily by the naphthalene bridging moiety. This leads to two unique iron(II) centres in the asymmetric unit. The DME solvent molecules are orientated either parallel or perpendicular to the plane of the central naphthalene moiety (ESI, Fig. S2). As these spaces are occupied by the DME molecules, any possible π-π interactions are prevented from occurring between the naphthalene rings or between the naphthalene rings and any pyrazolyl rings.

The DME solvent molecules form hydrogen bonds from oxygen to the C-H of the pyrazolyl ring and to some of the methylene groups in the complex. Weak C-H…F hydrogen- bonds between the BF_4^- anions, pyrazolyl hydrogen atoms of the ligand and MeCN solvent molecules are also observed. Overall, these supramolecular features help to assemble the 3D structure of the lattice but the lack of strong and direct supramolecular interactions between dinuclear complexes

probably translates into the lack of cooperativity being observed in the susceptibility measurements.

5.8MeCN.2^{t}BuOMe

Contained in the asymmetric unit are two non-identical iron(II) centres within the tetranuclear moiety, with each $Fe(N)_6$ coordination sphere being very similar to those observed for the previously described structures

Weak C-H---F hydrogen bond interactions are observed between the BF_4^- anions and the pyrazolyl hydrogen atoms and these are the predominant intermolecular force observed.

Notes on octahedral distortion parameters (reference numbers as in the script)

There are several ways to extract meaningful information about the interplay between the structural characteristics of the iron(II) centres and their SCO properties, in a prognostic manner. In general, crystallography can show quite distinctly the difference between the LS and HS states of iron(II) centres by observed changes in the Fe-N bond lengths with typical LS Fe-N bond lengths being *ca.* 1.9 Å whilst HS are typically *ca.* 2.2 Å. However, these measures are of little prognostic value, since they are a result of SCO, and provide little illumination on the intrinsic intramolecular parameters that indicate the likelihood of SCO occurring. A common intramolecular parameter used for such purposes in SCO studies is the octahedral distortion parameter (Σ), which examines the local angular distortion of the *cis* N-Fe-N angles (α_i) of the $Fe(N)_6$ coordination centre.[28] Calculating Σ is accomplished using Eq. 1.

$$\sum \square = \sum_{i=1}^{12} |90 - \alpha_i| \qquad (1)$$

Large values for Σ, a result of large angular distortions, generally associated with HS iron(II), can predispose the complex to a high probability of SCO inhibition as trapping of the HS state occurs, especially when $\Delta\Sigma$ is large. The calculated values of Σ for all structures in this study are low, which is not surprising, as all the structures display typical LS characteristics for $Fe(N)_6$ coordination centres and reflects well the observed magnetic properties at the measured temperatures. The values of Σ are reported in Table 5 and are all

close to 25º.

Examination of SCO and octahedral distortion can also be achieved by an alternative calculation using the trigonal distortion (Θ). This parameter is defined by measuring the 24 N-Fe-N angles (θ_j) from a projection of the two triangular faces of an octahedral centre along its pseudo-threefold axis (Eq.2).[29] The Θ parameter has been found to have a good correlation with the T(LIESST) for a spin transition. However, the $T_{1/2}$ for the compounds in this study is too high and the LIESST effect could not be observed.

$$\Theta = \sum_{j=1}^{24} |60 - \theta_j| \quad (2)$$

Values of Θ for all complexes are detailed in Table 5. The values are also typical of those displayed by LS iron(II), as they show little angular distortion from ideal octahedral coordination geometry. In an ideal octahedron both ∑ and Θ are zero. It is to be noted that in our earlier paper[13] on monomeric $[Fe((3,5\text{-}Me_2pz)_3CH)((pz)_3CH)](BF_4)_2$ type complexes we used a Θ expression divided by 24 and thus the quoted values are correspondingly much lower than those in Table 5. Interestingly, the Θ values observed here for the bis-tridentate tris-pyrazolylmethane coordination spheres are similar in size to those reported for tridentate/monodentate examples such as $[Fe((3,5\text{-}Me_2pz)_3CH)(NCS)_2(MeCN)]$ that remains in the HS state.[30]

Finally, the structural parameter τ, analyses the torsion angles of the metal-ligand framework, in particular the torsion angle generated through four atoms comprising the Fe(II) centre, the two nitrogen atoms of the pyrazolyl ring and the methine carbon. The value of τ, for mainly homoleptic complexes based on tris(pyrazolyl)methane and tris(pyrazolyl)hydridoborate ligands, does display a good relationship with SCO behaviour in these complexes. Notably, large values of τ coincided with SCO inhibition in HS tris(pyrazolyl)hydridoborate $[Fe(L)_2]$ derivatives.[31] When the τ parameter is applied to the mixed tripodal ligand sets found in the present study, the values of τ (<4º) are small, indicative of LS iron(II) centres in these polynuclear species (Table 1).

Mössbauer effect studies on compound 1 in the solvated and desolvated forms (reference numbers as in script)

Mössbauer effect measurements were made for samples of both **1.**2DME and **1** at 78 K and room temperature, temperatures at which the magnetism indicates low-spin behaviour. The spectrum of the desolvated sample, **1**, at room temperature is shown in Fig. S10 A. It can be seen that it is relatively featureless, but slightly asymmetrical and broadened and so that it could not be fitted to a simple Lorentzian or Voigtian profile. The majority of the spectrum was fitted to a Voigtian profile, with a correlation, δ_1, between the isomer shift (IS) and the quadrupole splitting (QS). A significantly better fit (χ^2 improved from 0.59 to 0.49) was obtained by assuming a Voigtian with two components and it is this fit which is shown, although both sets of parameters are given in Table 2 (script). Another broad Voigtian was required to cover the intensity out in the wings. This contribution is probably due to an impurity and occurs in all spectra. However, because of its broad spread and overlap with the main feature, it is not clear whether it is really a doublet with a QS ~ 1 mm/s or more, or a very broad distribution with a mean QS ~ 0, but a standard deviation of ~ 1 mm/s. Fits to various spectra usually preferred the latter, but we do not believe that the parameters for it are physically meaningful and so will not be further discussed.

To try and enhance the resolution, a room temperature spectrum was taken of a set of needle-shaped crystals of **1**, that retained their original morphology, and arranged lying down in the holder so that their axes were perpendicular to the gamma ray beam (Fig. S12 B). This spectrum can be seen to be more asymmetrical than that of the powder sample. Fitting it with a Voigtian for the main subspectrum and allowing the line intensities to vary, with a further Voigtian for the impurity gave a reasonable fit. The ratio of A_-/A_+ came out as 0.76, reasonably close to the expected value of 0.60 for the EFG axis perpendicular to the gamma ray beam in a perfect single crystal and a negative EFG.

Allowing the main subspectrum to have two components as in Fig. S12 A gave a 30% improvement in χ^2 with a further improvement if the two components were not tied to the same isomer shift. However, these possibilities produced a set of acceptable spectra because δ_1 and the peak ratios, A_-/A_+, are not independent with this limited resolution. The fit shown in Fig. S12B is under the same conditions as that in Fig. S12 A. The acceptable fits covered the range in δ_1 from 0 to -0.08 and in A_-/A_+ from 1.1 to 0.7.

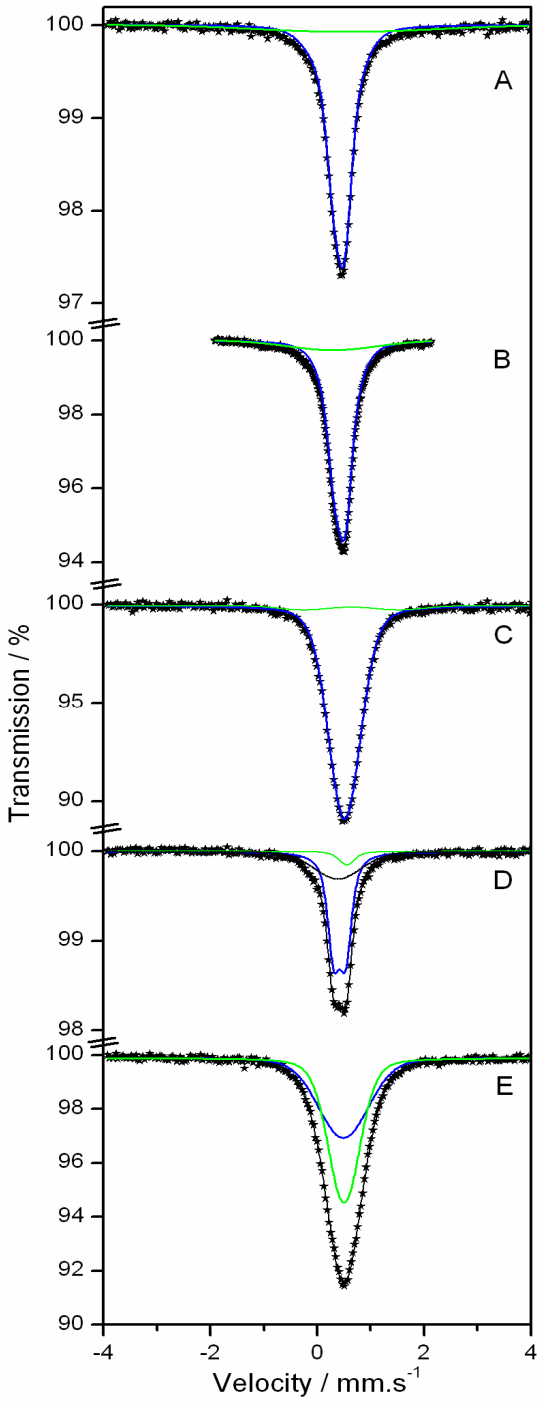

Fig. S12 Mössbauer spectra performed on compound **1**, powder form, at room temperature (A), **1** in crystal form at room temperature (B), **1** in powder form at 78 K (C), **1**·2DME at room temperature (D) and **1**·2DME at 78 K (E). Sub-spectra shown in colours.

The most probable interpretation of these Mössbauer results is that the structure contains two, very slightly different, iron configurations and the next nearest neighbour effects of these on their neighburs results in the correlated IS – QS broadening. It is also possible that these two distributions are an approximation to a small continuous distribution, but there is insufficient resolution to distinguish between these two possibilities. Reger *et al.*[11] have measured quadrupole splitting variations in a case where the crystallography, as determined by XRD, indicates a single site. This situation is straightforward to understand because quadrupole splittings are sensitive to nearest, and to a lesser extent, next nearest neighbour interactions and bond lengths and angles, while XRD will respond to such variations principally with the average structure over the X-ray coherence length.

The spectrum of the powdered desolvated sample at 78 K is shown in Fig. S12 C. It can be seen to be more symmetrical than the room temperature spectra and it has been fitted with a single Voigtian for the main part, plus another Voigtian for the impurity. It seems likely that the reduction in temperature has caused the two sites, or distribution of sites, as seen in the room temperature spectra, to condense into one.

A spectrum of the desolvated sample taken at 398 K, aimed at probing the HS-HS state of **1**, showed a complex pattern with at least eight lines, some of which were quite broad. Taking a subsequent spectrum at 78 K showed that the pattern there had broadened considerably compared to the previous run at this temperature, indicating partial decomposition. However, there were three sharp lines in the 398 K spectrum, one being a vestige of the room temperature spectrum and the other being a high spin doublet with parameters IS = 1.09(1) mm/s and QS = 2.93(3) mm/s, which we believe is attributable to the original desolvated sample in its high spin state.

The spectrum of the solvated sample, **1**.2DME, at room temperature showed a relatively narrow, asymmetrical quadrupole split doublet with some broadening in the wings (Fig S12 D). The broadening is believed to be due to an impurity and will not be further discussed. It is not clear how to fit the asymmetry because the sample is not a single crystal and a Gol'danskii-Karyagin effect of this magnitude is very unlikely. Consequently we have simply added a small single line with the understanding that it is the parameters of the main doublet which are the important features and these will not be appreciably altered under any

other assumptions. The other two components were fitted to Voigtian lineshapes with the parameters given in Table 2.

At 78 K, the spectrum of the solvated sample had broadened considerably and it was fitted to two Voigtians (Fig. S12 E). The parameters of the weaker Voigtian corresponded well to those in the room temperature spectrum, allowing for the expected thermal shift of 0.12 mm/s. Its intensity has increased considerably, although there is poor orthogonality between the fits to the two components so that the uncertainties are quite large. The weak singlet from the room temperature spectrum has disappeared, indicating that it really was somehow connected with the main doublet. However, the most important feature of this spectrum is the considerable broadening of the main doublet into a relatively structureless, symmetrical feature with a mean QS of zero but a standard deviation of 0.9 mm/s, four times the well-defined QS at room temperature. The interpretation of this requires a little care because the spectrum has been fitted with a Gaussian distribution of QS and hence, for a mean QS of zero, there should be an equal number of positive and negative QS. However, the same spectrum would be obtained with a distribution of just one half of the Gaussian distribution, which could be either the positive or negative half. Thus, the crystallographic interpretation is that the most probable configuration is a symmetrical one with zero QS, but flanked by a, possibly continuous, distribution of QS out to approximately 2 mm/s.

Scheme S1 **Scheme showing the ligand syntheses**

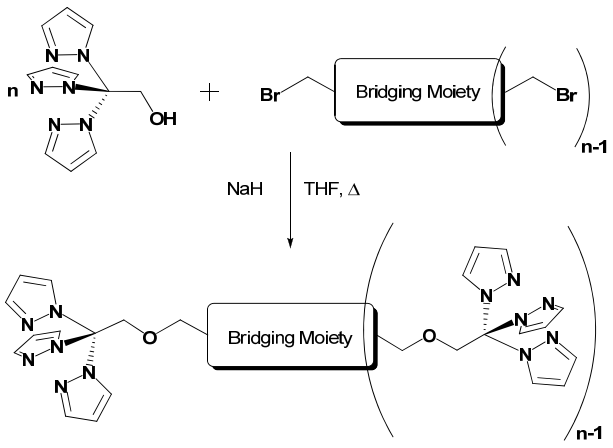

Scheme S1 Synthetic route for preparing ligands **L2** and **L3**